Electron shuttle of carboxyl boosted Fe(III)-anchored carboxylated cellulose activating sodium perborate for organic pollutant abatement

Shiyu Pan, Deling Yuan [*], Jinhao Li, Zhibin Wang, Qingrui Zhang [*], Shoufeng Tang [*]

State Key Laboratory of Metastable Materials Science and Technology, Hebei Key Laboratory of Heavy Metal Deep-Remediation in Water and Resource Reuse, School of Environmental and Chemical Engineering, Yanshan University, Qinhuangdao 066004, PR China

ARTICLE INFO

ABSTRACT

The traditional Fenton application is limited by the disproportionation of hydrogen peroxide (H_2O_2) and the tardy reduction of Fe(III). To conquer these issues, we construct an enhanced Fenton-like process using a composite of citric acid-carboxylated microcrystalline cellulose complexing with Fe(III) (CA-Fe(III)@MCC) to activate sodium perborate (SPB), which can effectively eliminate antibiotic sulfamethoxazole (SMX, 89.2%, 0.035 min^{-1}). The CA-Fe(III)@MCC composite significantly enhances the circulation of Fe(III)/Fe(II), leading to the generation of hydroxyl radicals and perboric radicals with excellent structural stability and minimal Fe leaching during CA-Fe(III)@MCC/SPB process. Systematic investigations reveal that the introduced carboxyl groups not only anchor Fe(III) to prevent its deactivation and leaching, but also regulate the coordination environment and serve as electron shuttles, driving the formation of reactive species and reduction of Fe(III). This process presents a novel, environmentally friendly, and sustainable strategy for utilizing natural cellulose and its industrial biomass product in advanced oxidation processes.

1. Introduction

The traditional Fenton method using ferrous ion (Fe^{2+}) and hydrogen peroxide (H_2O_2) can non-selectively decontaminate extensive organic pollutants via the generation of reactive oxygen species (ROS) [1]. Nevertheless, there are two main issues associated with conventional Fenton oxidation. One is that the easy disproportionation of H_2O_2 diminishes its role in the formation of ROS, and the instability of H_2O_2 raises the risks of storage and transportation [2]. Another is the sluggishness of ferric ion (Fe^{3+}) reduction, leading to the accumulation of Fe sludge and inactivation of Fenton reaction [3]. To conquer the key problem, a series of organic and inorganic reducing agents, such as low-molecular-weight organic acids and metal sulfides, are introduced to lower the redox reversibility of Fe^{3+}/Fe^{2+} through direct reduction or indirect complexation [4,5]. However, the potential application of these co-catalytic means is limited due to undesirable metal leaching, secondary pollution, and ROS quenching [6]. Therefore, the investigation of sustainability and environmentally friendly approaches aimed at achieving high-performance Fenton oxidation has garnered significant attention in the field of water pollution control.

Recently, solid peroxides such as persulfates and calcium peroxide (CP) have been increasingly used as substitutes for liquid H_2O_2 in advanced oxidation processes (AOPs) [7,8]. However, the high cost of persulfates and the issue of water hardening caused by calcium ions limit their widespread use [9,10]. Sodium perborate (SPB), a mild and nontoxic solid oxidant commonly used in aquaculture as an oxygen producer, slowly release H_2O_2 after dissolving in water, effectively avoiding the disproportionation of H_2O_2 and scavenging of ROS [11]. Recently, the replacement of H_2O_2 with SPB as an oxidant to construct a Fenton-like system has gradually garnered attention in AOPs [12]. Nevertheless, the sluggish conversion of Fe^{3+} to Fe^{2+} continues to be the rate-limiting step in the SPB-based Fenton-like process [13]. Additionally, the introduction of high concentrations of Fe^{2+} can quench free radicals, consequently diminishing the efficiency of pollutant removal [14]. Hence, iron-based heterogeneous catalysts present a viable alternative to mitigate these challenges.

Metal-free materials, such as carbonaceous materials (e.g., carbon nanotubes, graphite, and graphene) and biomass materials (e.g., biochar and natural cellulose), have been demonstrated to be suitable matrix materials for promoting Fe(III)/Fe(II) conversion in Fenton and Fenton-like reactions [15,16]. Therefore, the development of high-performing metal-free composites is a significant research focus. Surface

---

engineering is a typical strategy for modifying the surface chemistry properties and improving the catalytic reactivity of these metal-free complexes [17]. For example, doping nonmetals such as nitrogen, phosphorus, sulfur, and oxygen into carbon materials can alter the distribution density of charge, regulate the energy band structure, and then improve electron mobility and catalytic reactions [7,18]. Remarkably, Zhou et al. demonstrated that doping nitrogen onto carbon nanotubes resulted in the formation of carboxyl groups on the surface, which acted as electron suppliers for Fe(III) reduction, thereby enhancing Fenton oxidation efficiency [19]. Besides, introducing organic functional groups such as carbonyl, hydroxyl, and benzoquinonyl can chelate with metal ions and donate electrons to reduce high-valent metals [20,21]. Specifically, Zhang et al. found that carboxyl groups bonded to Fe(III) on the graphite surface, can promote persulfate adsorption to form surface complexes and induce electron transfer, accelerating heterogeneous Fenton-like reactions [22]. In other words, the surface modification through functional groups has been testified to be a rational way to enhance the activity of Fe(III) and the Fenton/Fenton-like reactions, with carbonyl groups playing a key role in mediating electrons. Cellulose is a typical polycarboxyl carrier that possesses abundant hydroxyl groups, providing numerous active sites for introducing carboxyl groups and enabling a higher loading of Fe(III) [23,24]. Cellulose, as a ubiquitous and low-cost natural polymer, is found in various forms, such as cotton, wood, and straw, and it offers exceptional thermal and chemical stability, water insolubility, renewability, and biodegradability, which has been proved to be a benign supporter for catalytic active substances [23,25]. Additionally, citric acid (CA) has been confirmed to be an effective chelator of Fe ions in homogeneous complexation Fenton/Fenton-like systems due to its carboxyl groups [26]. In comparison to other monocarboxylic and dicarboxylic acids, CA provides a greater number of sites for Fe(III) [27]. Furthermore, CA exhibited lower reactivity with ROS compared to oxalic acid and glutamic acid, decreasing the competitive reactions with the target organic compound for ROS [28,29]. Thus, CA is a promising candidate for bonding Fe(III) with the cellulose structure in heterogeneous Fenton/Fenton-like catalytic reactions. However, to the best of our knowledge, there is a noticeable research gap regarding the carboxylated cellulose composite anchoring Fe(III).

Hence, we synthesized a heterogeneous organic complexation composite via assembling citric acid-complexed Fe(III) with natural microcrystalline cellulose (CA-Fe(III)@MCC) to catalyze SPB Fenton-like reaction. Sulfamethoxazole (SMX) is a widely used antibiotic in aquaculture and is frequently detected in wastewater treatment effluents. Considering its potential threat to ecosystem and human health, SMX was selected as a model pollutant in this study. The main objectives of this study were to: (1) assess the performance of the proposed CA-Fe(III)@MCC/SPB process, (2) elucidate the role and mechanism of carboxyl groups in promoting Fe(III)/Fe(II) cycling, and identify the major forms of ROS in this heterogeneous system, (3) verify the stability and applicability of CA-Fe(III)@MCC, and explore the potential of natural cellulose and its industrial biomass product for practical water treatment.

2. Experimental section

2.1. Chemicals

Microcrystalline cellulose (MCC) and citric acid (CA, ≥99.5%) were purchased from Macklin Biochemical Co., Ltd, China. Sodium perborate (SPB, ≥97%) and sulfamethoxazole (SMX, 98%) were supplied by Aladdin Reagent Co., Ltd, China. The specified details of other chemicals utilized in this study are listed in Text S1 of the Supplementary Information (SI).

2.2. Fabrication and characterization of composites

Initially, 2.0 g of MCC was introduced into a 20 mL solution of CA

(0.5 mol/L). The resulting suspension was vigorously stirred for 30 min to ensure thorough mixing. Subsequently, the mixture was placed in a drying oven at 50°C for 7.5 h, followed by rapid heating to 120°C for a reaction time of 1.5 h. The CA@MCC composite was obtained by subjecting the reaction mixture to multiple washes with deionized water, removing any unreacted CA. Next, 2.0 g of CA@MCC was added to a 20 mL solution of $Fe(NO_3)_3 \cdot 9 H_2O$ (0.5 mol/L), and the resulting mixture was stirred for 12 h. The obtained solid powder was thoroughly washed several times and subsequently dried in an oven at 60°C for 24 h. This final product was designated as CA-Fe(III)@MCC. The similar synthetic procedure was employed to prepare the Fe(III)-loaded CA-modified cotton yarn (CA-Fe(III)@CY).

The surface morphologies, valence state, crystal structure, elemental composition and distribution, structural information, Fe leaching amount, and chemical properties of the catalysts were identified by scanning electron microscopy (SEM), X-ray photoelectron spectroscopy (XPS), X-ray diffraction (XRD), energy-dispersive X-ray spectroscopy (EDS), inductively coupled plasma optical emission spectroscopy (ICP-OES), Fourier-transform infrared spectroscopy (FTIR), and Raman spectroscopy, respectively. The detailed information of the used instruments was introduced in Text S2.

2.3. Experimental procedures

The catalytic activity experiments were conducted in a 50 mL beaker equipped with magnetic stirring at room temperature. To begin, a 5 mg/L solution of SMX was prepared, and the pH was adjusted using 0.1 mol/L H_2SO_4 and 0.1 mol/L NaOH. Subsequently, the predetermined CA-Fe(III)@MCC and SPB catalysts were simultaneously added to initiate the oxidation reaction. At specific time intervals, 1 mL of the reaction mixture was extracted and mixed with 1 mL of 1 mol/L methanol. The mixture was then filtered through a 0.22 μm PTFE filter for concentration analysis. All batch experiments were performed at least twice, and the average values with standard deviations were presented using error bars.

2.4. Analytical methods

The concentrations of methyl orange (MO) and rhodamine B (RhB) were detected by UV–visible spectrophotometer at 465 [30], and 554 nm [31], respectively. The concentrations of SMX, enrofloxacin (ENR), tetracycline (TC), dexamethasone (DXM), nitrobenzene (NB), metronidazole (MTZ), phenyl methyl sulfoxide (PMSO), and phenyl methyl sulfone (PMSO$_2$) were determined using high performance liquid chromatography (HPLC). The specific instrument information and HPLC analysis conditions are provided in Text S3 and Table S1, respectively. The degradation products of SMX were analyzed using mass spectrometry (MS), the detailed method was described in Text S4. The detailed detection methods of Fe content and H_2O_2 concentration are provided in Texts S5-S6, respectively. The content of carboxyl group was measured by potentiometric titration. The changes of crystallinity and functional groups were revealed by XRD and FTIR, respectively.

2.5. Electrochemical tests

The electrochemical measurements were conducted using an electrochemical workstation (CHI760E, Shanghai Huachen Instrument Co., Ltd, China) equipped with three-electrodes system [32]. The specified test processes were introduced in Text S7.

2.6. Quantum chemical calculation

All of the self-consistent periodic density functional theory (DFT) calculations were carried out using DMol3 code as implemented in the Materials Studio 2020 [33]. For geometry optimization, the convergence criteria for energy, maximum force, and maximum displacement

were set as 1×10^{-5} Ha, 2×10^{-3} Ha/Å, and 5×10^{-3} Å, respectively. The self-consistent field (SCF) convergence for each electronic energy was set as 1×10^{-6} Ha. The detailed computation method was show in Text S8.

3. Results and discussion

3.1. Synthesis and characterizations of CA-Fe(III)@MCC

The synthesis procedures of CA-Fe(III)@MCC are expounded in Fig. 1a, after the simple carboxylation, Fe(III) can be easily incorporated into cellulose by the normal temperature synthesis method. SEM was employed to examine the morphologies of MCC, CA@MCC, and CA-Fe (III)@MCC, revealing a rod-like structure (Figs. S1a-S1c). After anchoring Fe, the surface of CA@MCC exhibited a rougher texture with some lamellae, while maintaining the overall structure. The loading content of Fe in CA-Fe(III)@MCC was determined to be 3.26 wt% using

ICP-OES. Moreover, EDS analysis of CA-Fe(III)@MCC provided preliminary evidence of successful Fe incorporation without noticeable aggregation (Fig. S2).

Based on XRD results (Fig. 1b), all three samples exhibited the characteristic reflection planes of cellulose I ((−110), (110), (200), and (004)) [34], indicating that the chemical modification and Fe loading did not disrupt the cellulose structure. Furthermore, the carboxyl content of MCC was calculated as 0.173 mmol/g, which significantly increased to 0.533 mmol/g for CA@MCC (Text S9, Fig. S3, and Table S2), resulting in a proportional increase in the crystallinity index (CrI) from 74.5% to 77.0% (Fig. 1b). However, the CrI of CA@MCC decreased to 71.4% after the introduction of Fe. Importantly, no Fe oxides peak was observed in CA-Fe(III)@MCC. Therefore, Fe was chemically coordinated on the surface of CA@MCC through carboxyl groups [35].

FTIR spectra of the three samples also exhibited the characteristic absorption bands of cellulose I (Fig. 1c) [36]. The prominent band at
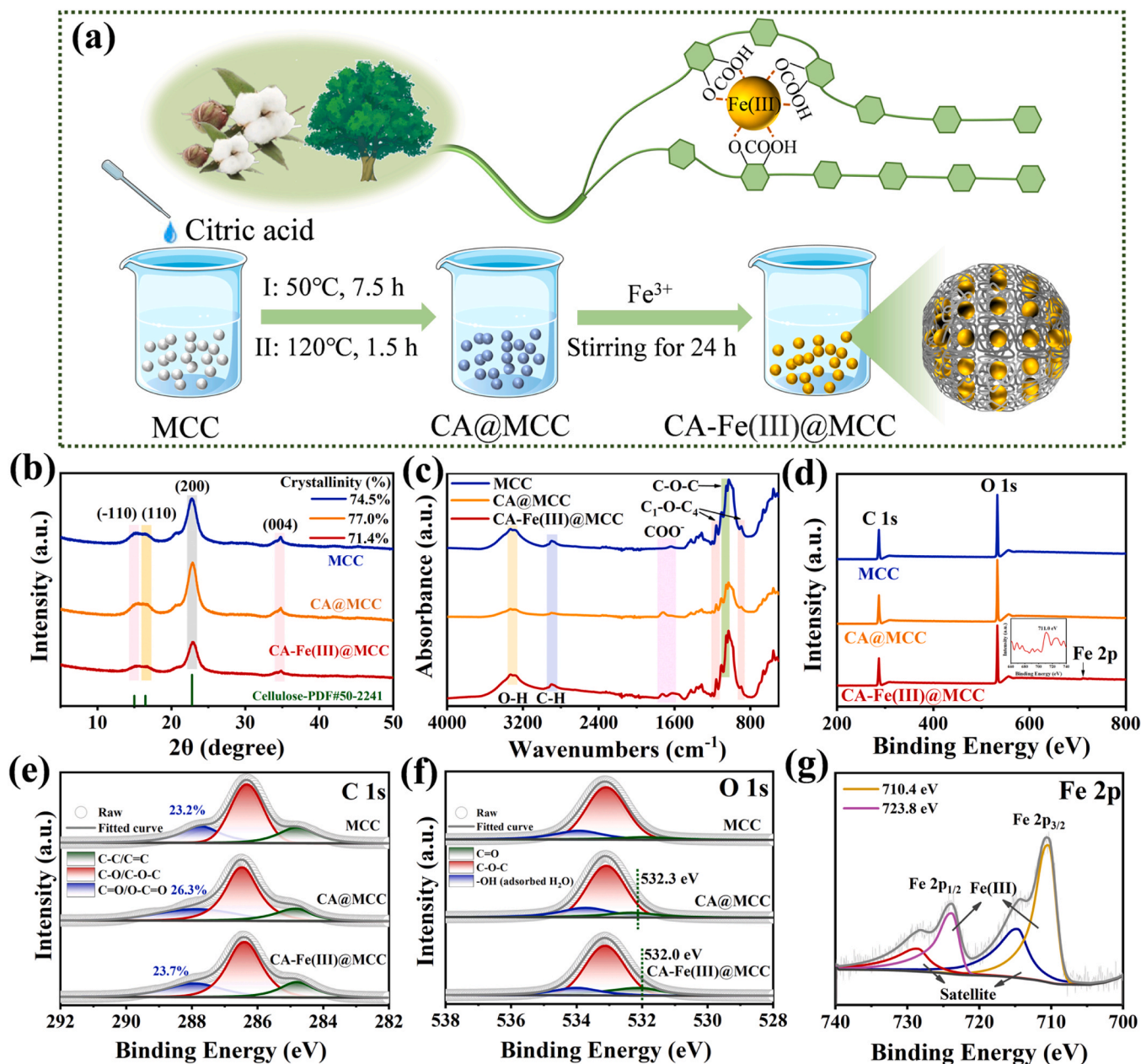

Fig. 1. (a) Schematic illustration of synthetic procedure for CA-Fe(III)@MCC. (b) XRD and (c) FTIR of MCC, CA@MCC, and CA-Fe(III)@MCC. (d-f) XPS full spectra, C 1 s, and O 1 s of different samples. (g) Fe 2p of CA-Fe(III)@MCC.

$1638\ cm^{-1}$ corresponded to the C=O stretching in MCC [37]. After introducing the ternary carboxylic acid structure and Fe, the C=O blue shift was observed in CA@MCC ($1718\ cm^{-1}$) and CA-Fe(III)@MCC ($1730\ cm^{-1}$). The shift of C=O stretching frequency and wavenumbers in CA-Fe(III)@MCC further confirmed the strong interaction between Fe and carboxyl groups [38].

XPS was further applied to investigate the chemical states of different elements. XPS full spectra in Fig. 1d confirmed the presence of C, O, and Fe in CA-Fe(III)@MCC. The weak Fe signal located at 711.0 eV could be ascribed to the low Fe loading. The enhanced atomic ratio of C=O in C 1 s (288.3 eV) of CA@MCC compared to MCC demonstrated the successful introduction of ternary carboxylic acid structure of CA (Fig. 1e) [39]. After integrating Fe onto CA@MCC, a distinct shift of C=O appeared in O 1 s spectrum of CA-Fe(III)@MCC (Fig. 1f), proving that the chemical state of C=O was changed after loading Fe. In Fig. 1g, the binding energy of Fe $2p_{3/2}$ (710.4 eV) exceeded that of Fe(II) phthalocyanine (FePc, 709.2 eV) and fell within the range of Fe(III) (709.8–711.8 eV) [40]. Hence, above characterizations collectively demonstrated that Fe(III) was integrated onto the surface of CA@MCC by coordinating with C=O of CA.

3.2. Catalytic performance of CA-Fe(III)@MCC/SPB

The catalytic performance of CA-Fe(III)@MCC/SPB process was assessed by removing SMX. In Fig. 2a, the minimal removals of SMX excluded the adsorption of CA@MCC and CA-Fe(III)@MCC, SPB oxidation, and the catalytic effect of CA@MCC on SPB. Previous studies have suggested that defects in carbon materials can induce catalytic activity [41]. Nevertheless, the absence of typical D and G bands in the Raman spectra (Fig. S4) explained the negligible catalytic effect of CA@MCC. In contrast, remarkable SMX removal (89.2%) was achieved within 60 min using CA-Fe(III)@MCC/SPB, with a rate constant (k_{obs}) of $0.035\ min^{-1}$, which was 87.5 times higher than that of Fe(III)@MCC/SPB ($0.0004\ min^{-1}$), highlighting the vital role of CA. Moreover,

a series of combination systems through simple additions without the preparation process (including CA/SPB, Fe^{3+}/SPB, MCC/SPB, CA/Fe^{3+}/SPB, Fe^{3+}/MCC/SPB, CA/MCC/SPB, and CA/Fe^{3+}/MCC/SPB) were compared with CA-Fe(III)@MCC/SPB (Fig. S5). The superior degradation capacity of CA-Fe(III)@MCC/SPB again demonstrated the advantage of our proposed composite. Furthermore, significant SMX degradation was also observed when coupling CA-Fe(III)@MCC with various solid peroxides (sodium percarbonate (SPC), CP, and peroxydisulfate (PDS)) (Fig. 2b), indicating the broad applicability of CA-Fe(III)@MCC for activating these representative solid peroxides.

Moreover, the degradation of SMX in CA-Fe(III)@MCC/SPB exhibited a positive feedback effect with increasing CA-Fe(III)@MCC dosage (Fig. 2c and S6a). However, excess SPB inhibited SMX decomposition (Fig. 2d and S6b), as the higher SPB dosage could release superfluous H_2O_2 to scavenge ROS. Additionally, as shown in Fig. 2e, CA-Fe(III)@MCC/SPB demonstrated high SMX degradation efficiency at pH 3.0. The reaction pH values decreased to some extent after adding CA-Fe(III)@MCC and SPB (Fig. S7). In addition, the zeta potential of CA-MCC ranged from pH 2.0–12.0 were more negative than that of MCC, indicating the successful introduction of negatively charged carboxyl groups (Fig. S8). After loading Fe(III), the zeta potential of CA-Fe(III)@MCC shifted towards a positive charge, which was negatively charged at pH>3.4. While SMX existed in amphoteric or anionic forms when the pH was higher than 3.4 (Fig. S9). Therefore, the electrostatic repulsion between the composite and SMX could hinder the removal of SMX when the pH was greater than 4.0 [42].

The SPB ($H_4B_2O_8^{2-}$) molecule dissolved in acid aqueous phase can readily convert to H_2O_2 via Eqs. (1) and (2) [11]. The decomposition of H_2O_2 was measured to primarily investigate SPB activation (Fig. 2f). SPB alone released 0.77 mmol/L H_2O_2. Remarkably, the concentration of H_2O_2 progressively decreased to 0.12 mmol/L in CA-Fe(III)@MCC/SPB, which was significantly lower than that of Fe(III)@MCC/SPB, demonstrating that the incorporation of CA into the Fe(III)@MCC framework prominently enhanced the catalytic reactivity.
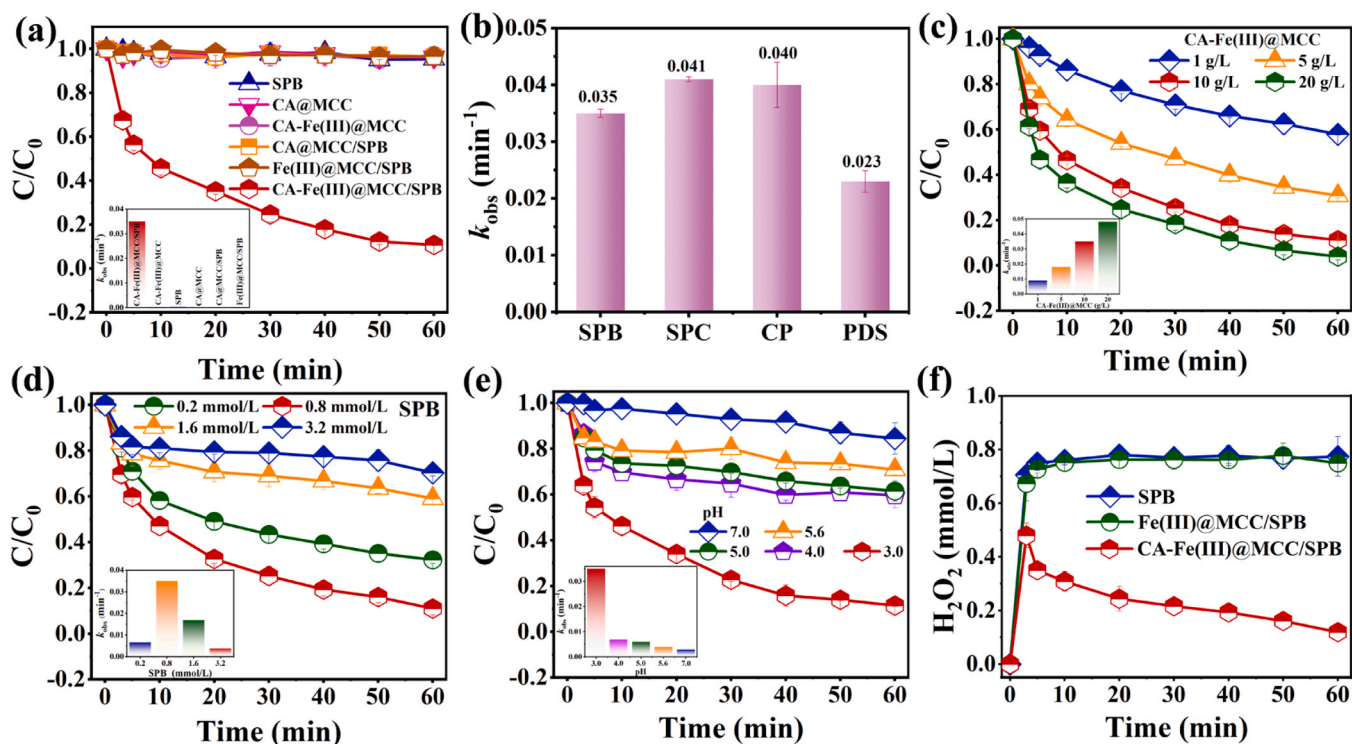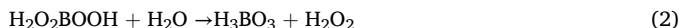

Fig. 2. (a) SMX elimination in diverse systems. (b) k_{obs} of different oxidants with CA-Fe(III)@MCC for SMX degradation. Effect of (c) CA-Fe(III)@MCC dosage, (d) SPB concentration, and (e) initial pH on SMX decomposition. (The inset of each figure is k_{obs} of SMX decomposition.) (f) Consumption of H_2O_2. ([CA-Fe(III)@MCC] = [Fe(III)@MCC] = [CA@MCC] = 10 g/L, [SPB] = [SPC] = [CP] = [PDS] = 0.8 mmol/L, [SMX] = 5 mg/L, pH_0 = 3.0).

$$H_4B_2O_8^{2-} + 2H^+ \rightarrow 2H_2O_2BOOH \tag{1}$$

$$H_2O_2BOOH + H_2O \rightarrow H_3BO_3 + H_2O_2 \tag{2}$$

3.3. Carboxylation function of CA-Fe(III)@MCC

The roles of CA were meticulously inspected to further explore the enhanced function of CA-Fe(III)@MCC. As illustrated in Fig. 3a, the increased SMX degradation with higher CA concentration during the composite preparation process could be attributed to the growing Fe(III) sites, which was also reflected in the reduced crystallinity of CA-Fe(III) @MCC as the CA concentration increased from 0.125 to 0.5 mol/L (Fig. 3b). However, the higher concentration of CA (1 mol/L) did not positively correlate with SMX degradation. It is possible that the increased crystallization region and decreased amorphous region of CA@MCC hindered the diffusion of Fe(III) and its coordination with carboxyl groups [43]. Furthermore, the leached Fe^{3+} was monitored during the reaction. Fig. 3c indicates that only 0.87 mg/L of Fe^{3+} was leached after 60 min, which accounted for 0.27 wt% of the Fe(III) loaded on CA-Fe(III)@MCC. This suggests that the strong complexing ability of CA with Fe(III) substantially prevents Fe leaching, reducing the loss and deactivation of Fe. Fig. S10 illustrates that the leached Fe^{3+} was unable to activate SPB, confirming that the heterogeneous reaction was dominant in CA-Fe(III)@MCC/SPB process.

Electrochemical tests were conducted to explore the action of CA in the Fe(III)/Fe(II) circulation from the perspective of electron mobility. The linear scanning voltammetry (LSV) analysis showed that the current response of CA-Fe(III)@MCC was stronger than that of Fe(III)@MCC (Fig. 3d). Cyclic voltammetry (CV) curves revealed that CA-Fe(III) @MCC displayed higher redox potential peaks and a larger area compared to Fe(III)@MCC (Fig. 3e), indicating that CA-Fe(III)@MCC had a greater electron storage capacity [44]. Besides, the electrochemical impedance spectroscopy (EIS) Nyquist arc diameter of CA-Fe (III)@MCC was visibly smaller than that of Fe(III)@MCC (Fig. 3f), demonstrating that CA-Fe(III)@MCC possessed a stronger electron transfer ability [45]. Moreover, according to the current response of MCC with or without CA upon adding Fe^{3+}, CA@MCC revealed a stronger current response (Fig. S11), which illustrated that the internal electron migration between CA@MCC and Fe^{3+} was more kinetically favorable due to the electron shuttle effect of CA [33].

Ulteriorly, the production of Fe(II) species was detected to further study the reducing function of CA. In Fig. 3g, hardly any Fe(II) species were observed in the suspension with Fe(III)@MCC. In contrast, CA-Fe (III)@MCC continuously generated Fe(II) species up to 0.48 mg/L
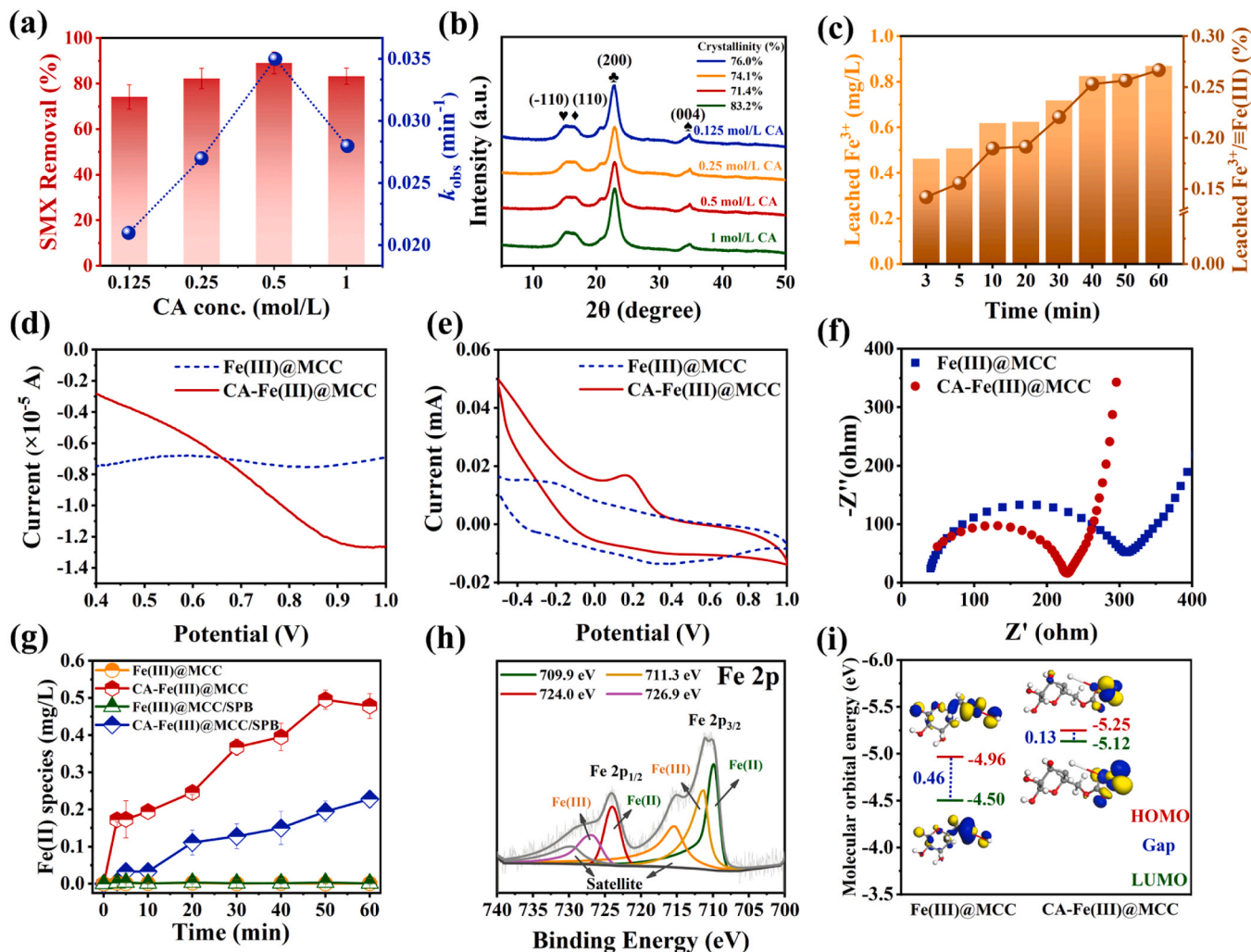
Fig. 3. (a) Effect of CA dose on SMX decomposition. (b) Crystallinity of CA-Fe(III)@MCC under different CA concentrations. (c) Fe(III) leaching content of CA-Fe(III) @MCC. (d-f) LSV, CV, and EIS analysis of CA-Fe(III)@MCC and Fe(III)@MCC. (g) Production of Fe(II) species. (h) Fe 2p spectra of CA-Fe(III)@MCC after reaction. (i) Gap between HOMO and LUMO of Fe(III)@MCC and CA-Fe(III)@MCC. ([CA-Fe(III)@MCC] = 10 g/L, [SPB] = 0.8 mmol/L, [CA] = 0.125–1 mol/L, [SMX] = 5 mg/L, $pH_0 = 3.0$).

after 60 min. The relatively small amount of Fe(II) species in CA-Fe(III) @MCC/SPB could be attributed to the rapid reaction with SPB. Additionally, the amount of Fe(II) species was found to increase with the concentration of CA (Fig. S12), demonstrating the pivotal role of CA in enhancing Fe(II) regeneration. Similarly, the inferior Fe(II) species at the higher CA concentration (1 mol/L) might be owed to the weak coordination of Fe(III) with higher crystallinity of CA [43]. In Fig. S13, the reduction of Fe(III) and SMX removal presented the same trend with the change of CA content, again proved the crucial role of CA. Besides, XPS spectra for Fe 2p after reaction revealed emerging peaks at 709.9 eV and 724.0 eV (Fig. 3h), which corresponded to Fe $2p_{3/2}$ and Fe $2p_{1/2}$ of Fe (II), respectively [46], validating the cycle of Fe(III)/Fe(II) on the composite surface. These results collectively certify that the introduction of CA directly contributes to the *in-situ* transformation of Fe(III) to Fe(II).

The interaction between CA@MCC (or MCC) and Fe(III) was studied using DFT simulation to highlight the thermodynamic advantage of the carboxylated composite. The electrostatic potential (ESP) diagrams of MCC with or without CA were calculated (Figs. S14a and S14b). The negative charge intensity of the carboxyl groups in CA@MCC was stronger than that of the hydroxyl groups in MCC, indicating that CA@MCC was more favorable for coordinating with the positively charged Fe(III) [47]. The optimal configurations of Fe(III)@MCC and CA-Fe(III)@MCC were displayed separately (Figs. S14c and S14d). The interaction energy between Fe(III) and MCC was -0.82 eV, but after introducing CA, the binding energy significantly increased to -4.35 eV. This enhanced interaction improves the internal electron transfer of the complex [40], as mirrored by the molecular orbital gap results. In Fig. 3i, the gap value of CA-Fe(III)@MCC (0.13 eV) was slightly lower than that of Fe(III)@MCC (0.46 eV), suggesting that the energy barrier of Fe(III) @MCC was reduced after introducing CA. This indicates that the electron is more easily transferred from the lowest unoccupied molecular orbital (LUMO) to the highest occupied molecular orbital (HOMO) in CA-Fe(III)@MCC [48]. In CA-Fe(III)@MCC, the amount of charge transferred from CA@MCC to Fe(III) was 0.30 e, which was higher than that of MCC to Fe(III) (0.23 e), further confirming that CA facilitates electron migration in MCC [49]. Based on the above findings, we can conclude that CA plays dual roles in CA-Fe(III)@MCC: (1) combining with Fe(III) to prevent Fe precipitation and catalyst deactivation; (2) acting as an electron shuttle to facilitate intramolecular electron transfer

and improve Fe(II) regeneration for mediating the catalytic reaction.

3.4. Identification of ROS in CA-Fe(III)@MCC/SPB

Tert-butanol (TBA), potassium iodide (KI), p-Benzoquinone (p-BQ), and L-Histidine (L-His) were applied as ROS quenchers for hydroxyl radical (HO·), surface HO· (HO·$_{surf}$), superoxide radical (O$_2^{\bullet-}$), and singlet oxygen ($^1O_2$), respectively, with respective rate constants ($k_{HO\bullet, TBA} = (3.8-7.6) \times 10^8 \text{ M}^{-1}\cdot\text{s}^{-1}$, $k_{HO\bullet surf, KI} = 1.2 \times 10^{10} \text{ M}^{-1}\cdot\text{s}^{-1}$, $k_{O2\bullet-, p-BQ} = 1.0 \times 10^9 \text{ M}^{-1}\cdot\text{s}^{-1}$, $k_{1O2, L-His} = 3.2 \times 10^7 \text{ M}^{-1}\cdot\text{s}^{-1}$) [50–52]. The addition of TBA led to a noticeable discernible inhibition of SMX decomposition, confirming the key role of HO· (Fig. 4a). In Fig. 4b, the evident restraint in SMX removal with 10 mmol/L KI implied that the HO·$_{surf}$ was the dominant ROS during the heterogeneous reaction. Fig. 4c showed that SMX elimination decreased to 63.5% after adding 5 mmol/L p-BQ. However, the drastic decline of 7-hydroxycoumarin peaks in coumarin fluorometry under 5 mmol/L p-BQ demonstrated the quenching effect of p-BQ on HO· (Figs. S15a and S15b) [53]. Besides, it was known that O$_2^{\bullet-}$ could not directly oxidate organics due to its weak oxidation capacity (−0.20 V) [54]. In Fig. 4d, the decomposition of SMX visibly dropped to 32.9% with 1 mmol/L of L-His. Significantly, L-His also had a high reactivity with HO· ($k_{HO\bullet, L-His} = 7.1 \times 10^9 \text{ M}^{-1}\cdot\text{s}^{-1}$) [52]. Therefore, considering the similar order of magnitude, the masking difference between TBA (10 mmol/L) and L-His (1 mmol/L) can represent the role of $^1O_2$, and the inconspicuous discrepancy proved the nonsignificant effect of $^1O_2$. Above results preliminarily proved the dominant role of HO·. In addition, electron paramagnetic resonance (EPR) was applied to reconfirm the existence of ROS. In Figs. 4e-4g, the strong signals of 5,5-dimethyl-1-pyrroline-N-oxide (DMPO)-HO· (1:2:2:1), DMPO-O$_2^{\bullet-}$ (1:1:1:1), and 2,2,6,6-tetramethylpeperidine (TEMP)-$^1O_2$ (1:1:1) adducts manifested the formations of HO·, O$_2^{\bullet-}$, and $^1O_2$ in CA-Fe(III)@MCC/SPB, respectively [55,56]. The specific contributions of these ROS need further exploration.

Recent studies have suggested the involvement of high-valent iron-oxo (Fe^{IV}=O) species in iron-based heterogeneous Fenton reactions [57]. PMSO was applied as the chemical probe to determine the formation of Fe^{IV}=O species [58]. Fig. S16 presents PMSO was hardly reduced and no PMSO$_2$ was produced, suggesting that Fe^{IV}=O was not involved in this process [57]. Furthermore, NB and MTZ were used as the probes of HO· and $^1O_2$, respectively, to determine their contributions
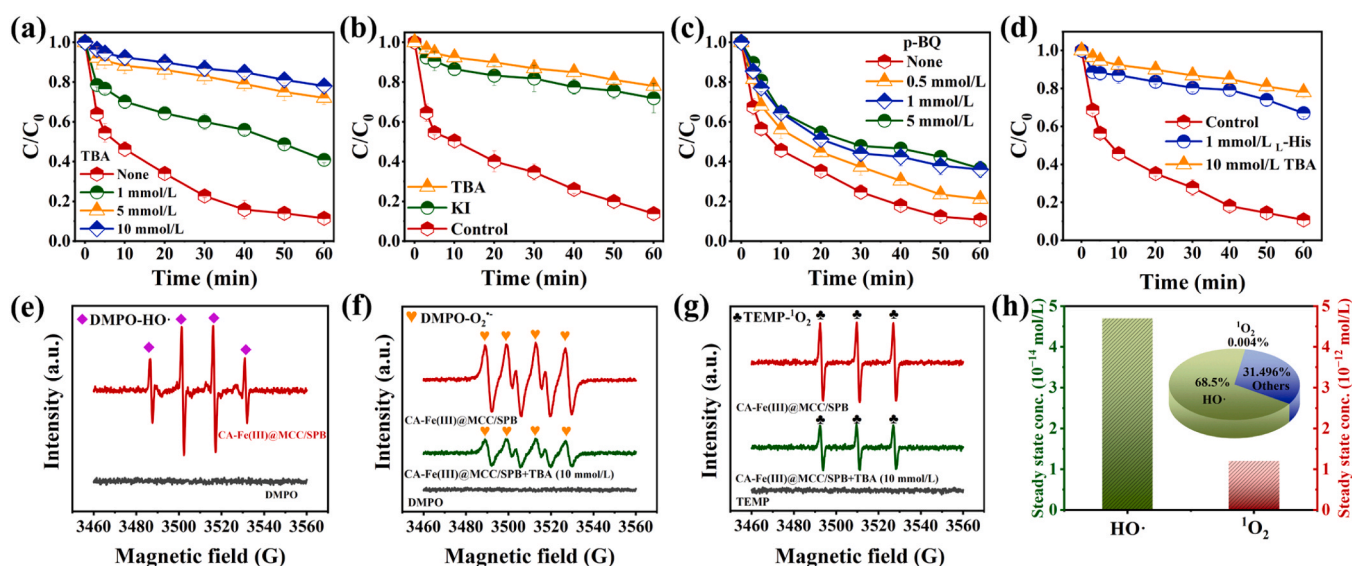
Fig. 4. (a-d) Effect of different radical quenchers including TBA, KI, p-BQ, and L-His on SMX elimination under CA-Fe(III)@MCC/SPB. (e-g) EPR spectra of DMPO-HO·, DMPO-O$_2^{\bullet-}$, and TEMP-$^1O_2$ adducts. (h) Steady state concentrations and contributions of HO· and $^1O_2$ to SMX degradation in CA-Fe(III)@MCC/SPB system. ([CA-Fe(III)@MCC] = 10 g/L, [SPB] = 0.8 mmol/L, [SMX] = 5 mg/L, [TBA] = 1−10 mmol/L, [L-His] = 1 mmol/L, [p-BQ] = 0.5−5 mmol/L, [KI] = 10 mmol/L, pH$_0$ = 3.0).
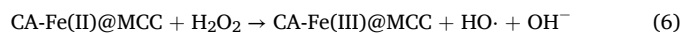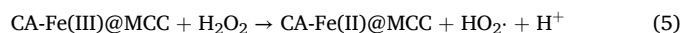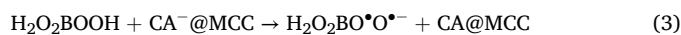
[52,59]. The second-order rate constants for the probes with HO· and $^1O_2$ are listed in Table S3. In Fig. S17, the k_{obs} of NB and MTZ degradation in CA-Fe(III)@MCC/SPB system were 0.011 and 0.021 min^{-1}, respectively. Based on this, the steady state concentrations of HO· and $^1O_2$ were computed to be 4.7×10^{-14} and 1.2×10^{-12} mol/L, separately (Eqs. S6-S13 in Text S10). Although the steady state concentrations of $^1O_2$ was 100 times of HO·, the second-order rate constant of HO· (8.5×10^9 M^{-1} s^{-1}) with SMX was 10^5 times higher than that of $^1O_2$ (2.0×10^4 M^{-1} s^{-1}) [52]. Therefore, the contributions of HO· (68.5%) on SMX degradation was much higher than that of $^1O_2$ (0.004%) (Fig. 4 h). Thus, it can be concluded that HO· was the critical ROS for SMX removal in CA-Fe(III)@MCC/SPB, while the functions of Fe^{IV}=O, $O_2^{\bullet-}$, and $^1O_2$ can be neglected.

From above, it is reasonable to deduce the presence of other reactive species involved in SMX elimination. Zeng et al. and Ming et al. proposed that H$_2$O$_2$BOOH reacts with strongly electrophilic ionized permonosulfate (SO_5^{2-}) to produce the strong electrophilic perboric radical (H$_2$O$_2$BO$^\bullet$O$^{\bullet-}$), which could attack organic contaminants via double-electron electrophilic effect [11,60]. In our process, CA$^-$@MCC possessed strong electrophilicity due to the exposure of carboxylate ions (COO$^-$) after leaching Fe(III), allowing it to react with H$_2$O$_2$BOOH to yield the electrophilic H$_2$O$_2$BO$^\bullet$O$^{\bullet-}$ (Eq. (3)).

To further explore the mutual conversion of ROS in the chain reaction, EPR analyses were conducted in the existence of superfluous TBA. Fig. 4 f and 4 g show that the intensities of DMPO-O$_2^{\bullet-}$ and TEMP-$^1O_2$ were much weaker after adding excess TBA compared to CA-Fe(III) @MCC/SPB without a quenching agent, implying that HO· contributed to the production of $O_2^{\bullet-}$ and $^1O_2$.

In summary, the evolution mechanism of ROS can be described as follows: Initially, SPB is converted to H$_2$O$_2$BOOH under the acidic circumstance (Eq. (1)), then gradually split into H$_2$O$_2$ (Eq. (2), Fig. 2f). For CA-Fe(III)@MCC, the ground-state Fe(III) can ensure the stability of composite material. The carboxyl groups served as the electron shuttle, driving the reduction of Fe(III) through intermolecular electron transfer and promoting the generation of excited Fe(II) (Eq. (4), Figs. 3g and 3h), which served as the primary active site to activate SPB for the generation of HO· for removing SMX (Eqs. (5)-(6), Fig. 2f, 4a and 4e). Although $O_2^{\bullet-}$ and $^1O_2$ are derived from the chain reactions of HO· (Fig. 4 f and 4 g), they hardly participated in SMX removal (Eqs. (7)-(9), Figs. 4c and 4 h) [3,61]. On the other hand, Fe(III) is leached gradually during the

catalytic reaction, then the electrophilic CA$^-$@MCC easily interacts with H$_2$O$_2$BOOH to form H$_2$O$_2$BO$^\bullet$O$^{\bullet-}$ through electrophilic substitution (Eq. (3)), thereby advancing SMX degradation. Overall, the CA acts as the essential electron shuttle, facilitating the internal electron transfer of CA-Fe(III)@MCC (Figs. 3d-3f), promoting the regeneration of excited Fe (II) and the excitation of SPB synchronously.

$$H_2O_2BOOH + CA^-@MCC \rightarrow H_2O_2BO^\bullet O^{\bullet-} + CA@MCC \quad (3)$$

$$CA\text{-}Fe(III)@MCC \rightarrow CA\text{-}Fe(II)@MCC \quad (4)$$

$$CA\text{-}Fe(III)@MCC + H_2O_2 \rightarrow CA\text{-}Fe(II)@MCC + HO_2\cdot + H^+ \quad (5)$$

$$CA\text{-}Fe(II)@MCC + H_2O_2 \rightarrow CA\text{-}Fe(III)@MCC + HO\cdot + OH^- \quad (6)$$

$$H_2O_2 + HO\cdot \rightarrow HO_2\cdot + H_2O \quad (7)$$

$$HO_2\cdot \rightarrow H^+ + O_2^{\bullet-} \cdot \quad (8)$$

$$O_2^{\bullet-} + HO\cdot \rightarrow {}^1O_2 + OH^- \quad (9)$$

3.5. In-depth catalytic mechanism of CA-Fe(III)@MCC

DFT calculation was further applied to distinguish the catalytic mechanism at molecular level. The optimized configurations of H$_2$O$_2$ and SPB are displayed in Figs. 5a and 5b, respectively, while Figs. 5c and 5d show the optimal adsorption configurations of H$_2$O$_2$ and SPB on CA-Fe(III)@MCC, respectively. The interaction energies of the adsorbed H$_2$O$_2$ and SPB on CA-Fe(III)@MCC were determined to be −8.15 eV and −4.78 eV, respectively. The larger interaction energy indicates faster electron transfer between H$_2$O$_2$ and CA-Fe(III)@MCC [32], which was also reflected by the sharp increase in open circuit potential (OCP) upon adding H$_2$O$_2$ (Fig. S18). Whereas, only 41.3% of SMX was eliminated in CA-Fe(III)@MCC/H$_2$O$_2$ (Fig. S19), which was much less than the removal efficiency observed in CA-Fe(III)@MCC/SPB. Moreover, based on the results of coumarin fluorometry (Figs. S15a and S15c), the yield of HO·in CA-Fe(III)@MCC/H$_2$O$_2$ during the first 10 min was higher than that in CA-Fe(III)@MCC/SPB but decreased significantly in the last 50 min. Based on the results of theoretical calculations and experimental analysis, the stronger adsorption of H$_2$O$_2$ on CA-Fe(III)@MCC leads to the rapid formation of HO·, resulting in the self-quenching reaction
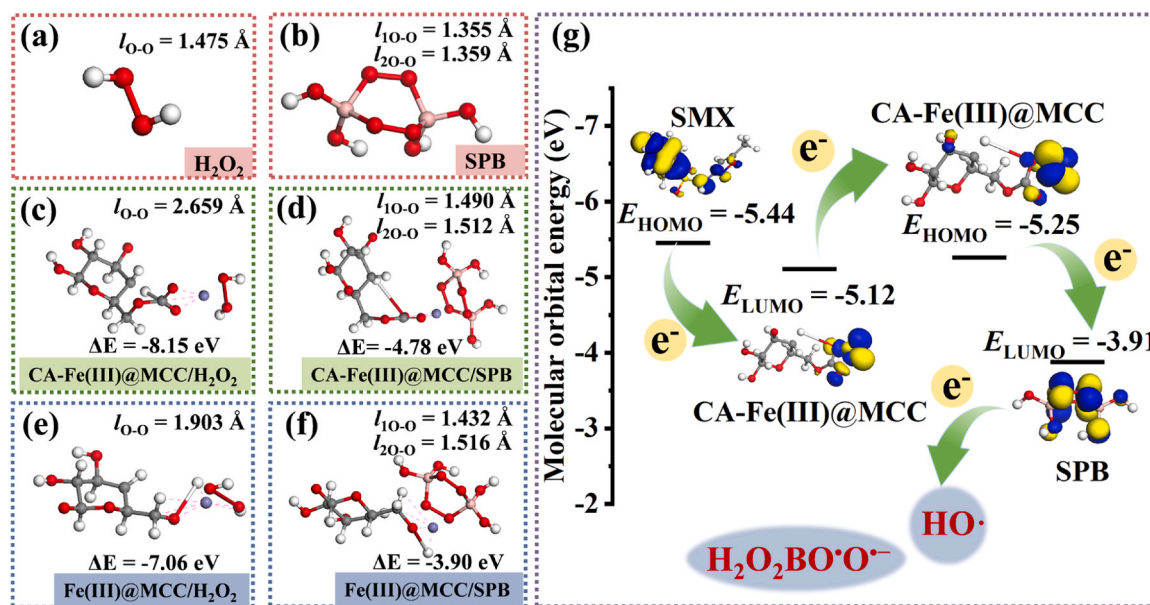

Fig. 5. (a, b) Optimal configurations of H$_2$O$_2$ and SPB. (c, d) Optimal adsorption configurations of H$_2$O$_2$ and SPB on CA-Fe(III)@MCC. (e, f) Optimal adsorption configurations of H$_2$O$_2$ and SPB on Fe(III)@MCC. (g) Possible electron transfer mechanism in CA-Fe(III)@MCC/SPB.

between H_2O_2 and HO· (Eq. (7)). In contrast, the slow release of H_2O_2 from SPB enables continuous adsorption and catalysis by CA-Fe(III) @MCC, resulting in stable HO· production. Thus, SPB was deemed as a more suitable oxidant than H_2O_2 for the catalytic oxidation of CA-Fe (III)@MCC.

Further, the adsorption configurations of H_2O_2 and SPB on Fe(III) @MCC were optimized to elucidate the role of CA. In Figs. 5e and 5 f, the adsorption energies of H_2O_2 and SPB on Fe(III)@MCC were determined to be −7.06 eV and −3.90 eV, respectively, which were weaker than those on CA-Fe(III)@MCC (−8.15 eV and −4.78 eV, Figs. 5c and 5d). Therefore, the introduction of CA could improve the interaction between Fe(III) and SPB on MCC, resulting in the enhanced electron migration. Consequently, we proposed the possible electron transfer pathway in Fig. 5 g. The electrons derived from the HOMO of SMX (-5.44 eV) can readily transfer to the LUMO of CA-Fe(III)@MCC (-5.12 eV). Subsequently, within CA-Fe(III)@MCC, the electrons can easily migrate from the LUMO to the HOMO due to the low energy barrier. Ulteriorly, the electrons centered on the HOMO of CA-Fe(III)@MCC (-5.25 eV) were transmitted to the LUMO of SPB (−3.91 eV), launching an electrophilic attack to the O-O bond of SPB for the generation of ROS and subsequent removal of organic pollutant.

3.6. Application potential of CA-Fe(III)@MCC

A series of experiments were implemented to examine the reusability and stability of CA-Fe(III)@MCC. Fig. 6a demonstrates a distinct decline in SMX removal after the tenth cycle of CA-Fe(III)@MCC (59.1%), which might be attributed to the leaching of Fe(III) after each cycle (Fig. 6b). Therefore, CA-Fe(III)@MCC was simply regenerated by stirring in Fe $(NO_3)_3$·9 H_2O solution to recover its catalytic activity. Although the catalytic performance of CA-Fe(III)@MCC (73.5%) was partially recovered certainly after the regeneration (Fig. 6a), the more efficient regeneration method for this composite should be further investigated in future. Notably, the physical and chemical structures of CA-Fe(III) @MCC remained intact after the cyclic reaction, as confirmed by SEM (Fig. S1d), XPS (Figs. S20), and FTIR (Fig. S21a) analyses, testifying satisfactory stability of this composite. Nevertheless, the increased CrI of CA-Fe(III)@MCC (from 71.4% to 72.6%) after the reaction indicated the exposure of carboxyl due to leached Fe(III) (Fig. S21b). Moreover, two modes of continuous degradation tests were performed to reconfirm the stability of CA-Fe(III)@MCC: direct addition of 4 mmol/L SPB and stepwise addition of 4 mmol/L SPB divided into five equal parts. Fig. 6c illustrates that there was a slight difference in SMX elimination between the two methods, once again confirming the negligible self-quenching of SPB. The efficient removal (94.5%) of high-concentration SMX (25 mg/
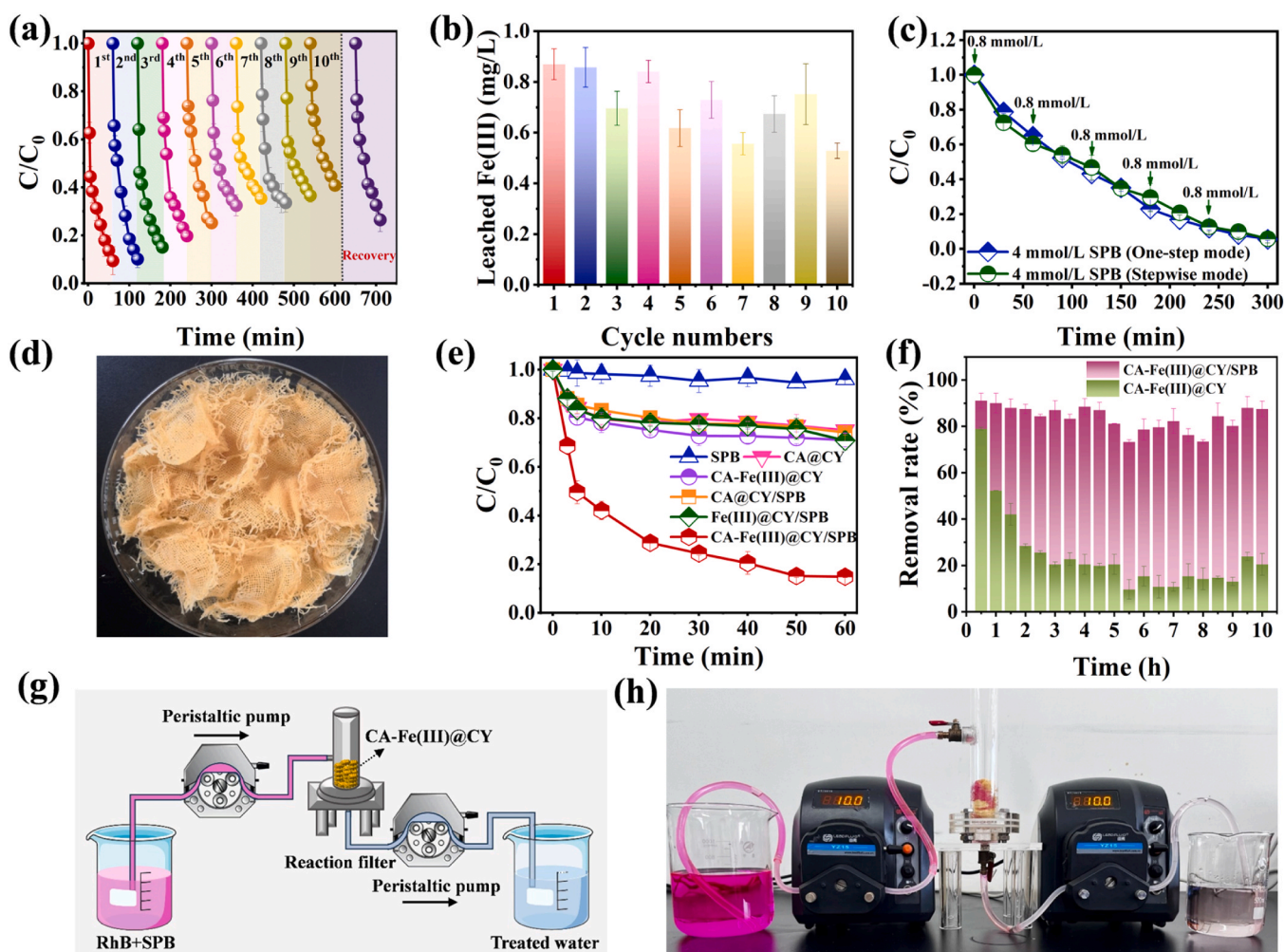
Fig. 6. (a) Ten cycles tests for SMX degradation. (b) Fe(III) leaching of each cycle. ([CA-Fe(III)@MCC] = 10 g/L, [SPB] = 0.8 mmol/L, [SMX] = 5 mg/L, pH$_0$ = 3.0). (c) Continuous degradation of SMX by CA-Fe(III)@MCC/SPB process in two modes. ([CA-Fe(III)@MCC] = 10 g/L, [SPB] = 4 mmol/L, [SMX] = 25 mg/L, pH$_0$ = 3.0). (d) Finished product of CA-Fe(III)@CY and (e) SMX removal in different systems. ([CA-Fe(III)@MCC] = [CA-Fe(III)@CY] = 10 g/L, [SPB] = 0.8 mmol/L, [SMX] = 5 mg/L, pH$_0$ = 3.0). (f) A self-regulating column reactor for removing RhB simulated wastewater during 10 h. (g, h) Diagram of dynamic removal test and corresponding photograph of microreactor. ([CA-Fe(III)@CY] = 6 g, [SPB] = 2.4 mmol/L, [RhB] = 2.5 mg/L, pH$_0$ = 3.0).

L) after 300 min proved the remarkable sustained catalytic capacity. The excellent reusability and stability CA-Fe(III)@MCC also could be ascribed to the strong complexing capacity of CA.

Furthermore, CA-Fe(III)@MCC/SPB exhibited non-selective degradation of various organic dyes and pharmaceuticals, including MO, ENR, TC, DXM, and RhB (Fig. S22). Besides, this established process demonstrated anti-interference capacity against low concentrations of Cl^-, NO_3^-, SO_4^{2-}, humic acid (HA), and HCO_3^-, except for HPO_4^{2-} (Fig. S23a), which readily chelates with Fe(III) and occupies active sites [62]. Hence, the less elimination of SMX in actual waterbodies could be related to the influences of inorganic anions and natural organic matters (Fig. S23b). In addition, the removals of COD and TOC achieved 20.6% and 16.1%, respectively (Figs. S24 and S25, Text S11). A comparison with other representative heterogeneous reducing agent-based Fenton-like systems (Table S4) was conducted, including iron-based heterogeneous systems, organic acid-modified systems, and carbon material catalytic systems. The results indicated that CA-Fe(III)@MCC/SPB exhibited comparable degradation performance with a minimal oxidant requirement. In addition, the cost and performance for CA-Fe(III)@MCC to similar materials (including chitosan-based and lignin based materials) were also compared (Table S5), the constructed CA-Fe(III)@MCC/SPB process presented a better cost-effectiveness ratio, which could be due to the simpler synthesis process.

For the engineering application potential of our proposal, a complex composite was prepared using cotton yarn as the carrier instead of MCC to test its catalytic performance (Fig. 6d). The engineered composite (CA-Fe(III)@CY) demonstrated the ability to activate SPB and remove 85.1% of SMX after 60 min, with a k_{obs} value of 0.029 min^{-1} (Fig. 6e and S26). Furthermore, a fixed-bed column reactor packed with CA-Fe(III)@CY was assembled for continuous wastewater treatment. RhB (2.5 mg/L) was used as an analog contaminant for observation (Figs. 6f-6h). As seen in Fig. 6f, in the first 0.5 h, CA-Fe(III)@CY exhibited certain adsorption capacity for RhB, which decreased significantly after reaching adsorption saturation. Notably, the decolorization efficiency remained above 70% during continuous operation after 10 h. Overall, CA-Fe(III)@MCC and CA-Fe(III)@CY demonstrated great potential for practical applications, with the expansion of the carrier from cellulose compounds in the laboratory to industrial product cotton yarn, presenting a promising perspective for the application of this Fenton-like process.

3.7. SMX degradation pathways and toxicity evaluation

The possible degradation evolution of SMX was proposed based on the MS (Fig. S27 and Table S6) and DFT calculations. Regions with negative charges, high HOMO orbitals, high f^0 and f^- values were found to be susceptible to HO· and electrophilic $H_2O_2BO^•O^{•-}$ (Figs. 7a-7c, and Table S7). Therefore, the byproducts were mainly produced through hydroxylation and sulfonamide bond cleavage reactions (Fig. 7d). In pathway I, the ortho-position (C4) of amino group was attacked by HO· to produce mono-hydroxylated SMX (P1, $m/z = 269.6$) [63]. Subsequently, the cleavage of S10-N13 of P1 and further hydroxylation resulted in the production of P2 ($m/z = 188.9$) [64]. In pathway II, the direct cleavage of S10-N13 of SMX resulted in the formation of sulfonic acid byproduct P3 ($m/z = 158.9$) and amine P5 ($m/z = 99.1$) [65]. Further, due to the attack of HO·, P3 and P5 underwent hydroxylation to produce P4 ($m/z = 172.7$) and P6 ($m/z = 114.8$), respectively [66]. The amino ortho position (C2 or C4) of byproduct P4 was readily attacked by HO· to form P2 [64]. Finally, some intermediates were mineralized into CO_2 and H_2O. To further prove the decomposition and mineralization of SMX, anti-bacteria test was conducted. As shown in Fig. 7e and Text S12, the decreased Escherichia coli (E. Coli) inhibition zones after treatment testified the decline of biotoxicity for SMX degraded byproducts. Computational toxicology results reconfirmed the reduced biotoxicities of SMX and its decomposed intermediates (Text S13 and Fig. S28).

4. Conclusions

We successfully prepared a heterogeneous organic complexation composite by assembling CA with eco-friendly natural cellulose, and introduced carboxyl groups onto the surface of CA@MCC as coordination centers for the bonding of Fe(III). CA-Fe(III)@MCC effectively activated SPB, degrading 89.2% of SMX within 60 min at a kinetic rate of 0.035 min^{-1}. The suitable carboxyl content (0.533 mmol/g) played
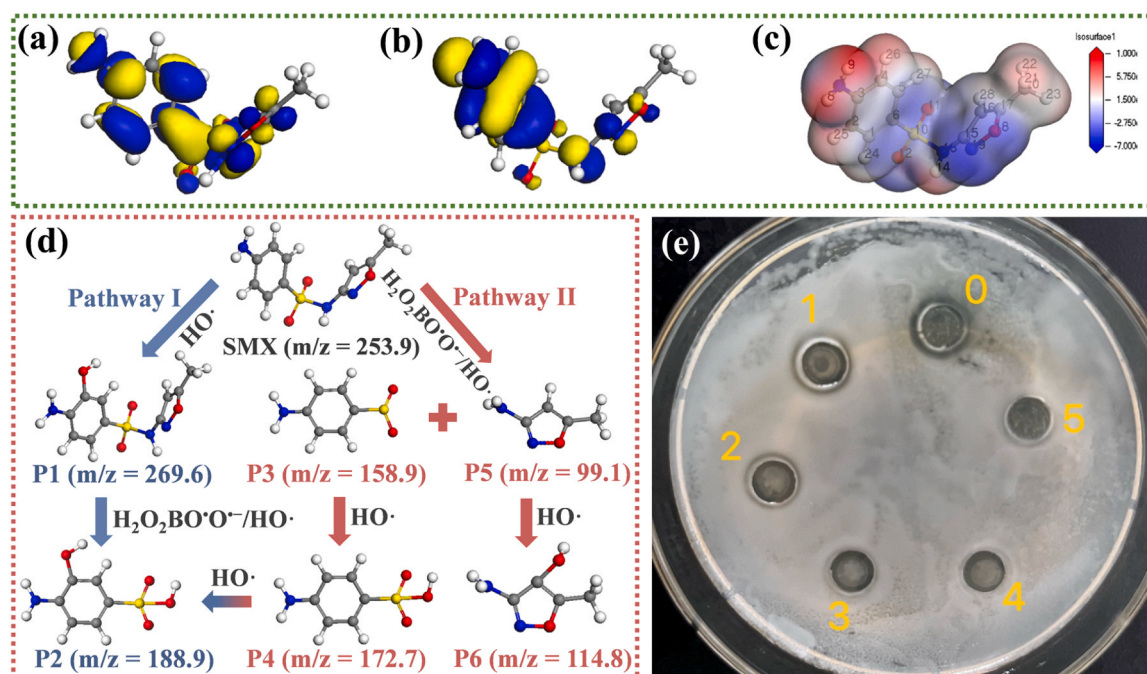
Fig. 7. (a) LUMO, (b) HOMO, and (c) ESP of SMX. (d) Possible pathways of SMX degradation by CA-Fe(III)@MCC/SPB. (e) Inhibition zones of *E. Coli* for SMX treated with different time (0–5: 0–5 h treatment by CA-Fe(III)@MCC/SPB). ([CA-Fe(III)@MCC] = 20 g/L, [SPB] = 1.6 mmol/L, [ΔOD600] = 0.091, [SMX] = 100 mg/L).

pivotal roles by anchoring Fe(III) on the surface of cellulose to regulate the coordination environment, prevent Fe leaching and precipitation, redistribute the energy barrier, and mediate electron transfer to enhance the effective conversion of Fe(III)/Fe(II). Theoretical simulations and systematical experiments unveiled that $HO·_{surf}$ was the dominant ROS contributing to SMX elimination, followed by $H_2O_2BO^{•}O^{•-}$. The slow release of H_2O_2 from SPB benefited its activation by CA-Fe(III)@MCC, resulting in stable ROS production, thus demonstrating that SPB was a more suitable oxidant than H_2O_2 in this Fenton-like reaction. The established Fenton-like system demonstrated favorable environmental adaptability and cycle stability, meanwhile, the synthesized cotton yarn-based composite possessed significant potential for future application. This work shed a new light for the utilization of natural and artificial biomass materials in wastewater treatment. Nevertheless, the optimization of preparation process for efficiently loading Fe is still required for the proposed composite, and further investigation is necessary for its recovery and regeneration in actual scenario.

CRediT authorship contribution statement

Qingrui Zhang: Writing – review & editing, Project administration, Funding acquisition. **Shoufeng Tang:** Writing – review & editing, Writing – original draft, Supervision, Project administration, Funding acquisition. **Shiyu Pan:** Writing – original draft, Investigation, Formal analysis, Data curation. **Deling Yuan:** Writing – review & editing, Project administration, Investigation, Funding acquisition, Conceptualization. **Jinhao Li:** Investigation. **Zhibin Wang:** Resources, Investigation.

Declaration of Competing Interest

The authors declare that they have no known competing financial interests or personal relationships that could have appeared to influence the work reported in this paper.

Data Availability

Data will be made available on request.

Acknowledgments

Appendix A. Supporting information

Supplementary data associated with this article can be found in the online version at doi:10.1016/j.apcatb.2024.124225.

References

[1] L. Chen, Z. Yang, J. Qian, B. Pan, Interaction between organic compounds and catalyst steers the oxidation pathway and mechanism in the iron oxide-based heterogeneous fenton system, Environ. Sci. Technol. 56 (2022) 14059–14068, https://doi.org/10.1021/acs.est.2c04557.

[2] J. Gao, X. Duan, K. O Shea, D.D. Dionysiou, Degradation and transformation of bisphenol A in UV/Sodium percarbonate: Dual role of carbonate radical anion, Water Res 171 (2020) 115394, https://doi.org/10.1016/j.watres.2019.115394.

[3] Z. Yang, C. Shan, J.J. Pignatello, B. Pan, Mn(II) acceleration of the picolinic acid-assisted fenton reaction: new insight into the role of manganese in homogeneous fenton AOPs, Environ. Sci. Technol. 56 (2022) 6621–6630, https://doi.org/10.1021/acs.est.1c08796.

[4] D. Yuan, C. Zhang, S. Tang, X. Li, J. Tang, Y. Rao, Z. Wang, Q. Zhang, Enhancing CaO_2 fenton-like process by Fe(II)-oxalic acid complexation for organic wastewater treatment, Water Res 163 (2019) 114861, https://doi.org/10.1016/j.watres.2019.114861.

[5] S. Pan, T. Zhao, H. Liu, X. Li, M. Zhao, D. Yuan, T. Jiao, Q. Zhang, S. Tang, Enhancing ferric ion/sodium percarbonate Fenton-like reaction with tungsten disulfide cocatalyst for metronidazole decomposition over wide pH range, Chem. Eng. J. 452 (2023) 139245, https://doi.org/10.1016/j.cej.2022.139245.

[6] H. Zhou, H. Zhang, Y. He, B. Huang, C. Zhou, G. Yao, B. Lai, Critical review of reductant-enhanced peroxide activation processes: Trade-off between accelerated Fe^{3+}/Fe^{2+} cycle and quenching reactions, Appl. Catal. B: Environ. 286 (2021) 119900, https://doi.org/10.1016/j.apcatb.2021.119900.

[7] B. Wu, Z. Li, Y. Zu, B. Lai, A. Wang, Polar electric field-modulated peroxymonosulfate selective activation for removal of organic contaminants via non-radical electron transfer process, Water Res 246 (2023) 120678, https://doi.org/10.1016/j.watres.2023.120678.

[8] S. Pan, B. Cao, D. Yuan, T. Jiao, Q. Zhang, S. Tang, Complexes of cupric ion and tartaric acid enhanced calcium peroxide Fenton-like reaction for metronidazole degradation, Chin. Chem. Lett. 35 (2024) 109185, https://doi.org/10.1016/j.cclet.2023.109185.

[9] S. Wu, L. Shen, Y. Lin, K. Yin, C. Yang, Sulfite-based advanced oxidation and reduction processes for water treatment, Chem. Eng. J. 414 (2021) 128872, https://doi.org/10.1016/j.cej.2021.128872.

[10] S. Seo, H. Jeon, J.K. Lee, G. Kim, D. Park, H. Nojima, J. Lee, S. Moon, Investigation on removal of hardness ions by capacitive deionization (CDI) for water softening applications, Water Res 44 (2010) 2267–2275, https://doi.org/10.1016/j.watres.2009.10.020.

[11] H. Zeng, X. Ling, J. Deng, L. Deng, H. Zhang, T. Shi, S. Zhou, Z. Shi, Activation of peroxymonosulfate via peroxyborate: Electrophilic substitution induced strong electrophile generation process, Chem. Eng. J. 451 (2023) 138925, https://doi.org/10.1016/j.cej.2022.138925.

[12] C. Zhang, Y. Dong, B. Li, F. Li, Comparative study of three solid oxidants as substitutes of H_2O_2 used in Fe (III)-oxalate complex mediated Fenton system for photocatalytic elimination of reactive azo dye, J. Clean. Prod. 177 (2018) 245–253, https://doi.org/10.1016/j.jclepro.2017.12.211.

[13] D. Xing, D. Shao, Y. Yang, Z. Zhou, G. Jing, X. Zhao, Mechanistic insights into the efficient activation of peracetic acid by pyrite for the tetracycline abatement, Water Res 222 (2022) 118930, https://doi.org/10.1016/j.watres.2022.118930.

[14] S. Xiao, M. Cheng, H. Zhong, Z. Liu, Y. Liu, X. Yang, Q. Liang, Iron-mediated activation of persulfate and peroxymonosulfate in both homogeneous and heterogeneous ways: A review, Chem. Eng. J. 384 (2020) 123265, https://doi.org/10.1016/j.cej.2019.123265.

[15] X. Duan, H. Sun, S. Wang, Metal-Free Carbocatalysis in Advanced Oxidation Reactions, Acc. Chem. Res. 51 (2018) 678–687, https://doi.org/10.1021/acs.accounts.7b00535.

[16] P. Zhang, P. Zhou, J. Peng, Y. Liu, H. Zhang, C. He, Z. Xiong, W. Liu, B. Lai, Insight into metal-free carbon catalysis in enhanced permanganate oxidation: Changeover from electron donor to electron mediator, Water Res 219 (2022) 118626, https://doi.org/10.1016/j.watres.2022.118626.

[17] W. Tian, H. Zhang, X. Duan, H. Sun, G. Shao, S. Wang, Porous Carbons: Structure-Oriented Design and Versatile Applications, Adv. Funct. Mater. 30 (2020) 1909265, https://doi.org/10.1002/adfm.201909265.

[18] C. Wang, B. Wei, H. Zhu, Y. He, G. Ran, Q. Song, Engineering FeS_2 nanoparticles on tubular g-C_3N_4 for photo-Fenton treatment of paint wastewater, Chin. Chem. Lett. 33 (2022) 3073–3077, https://doi.org/10.1016/j.cclet.2021.09.051.

[19] C. Zhou, P. Zhou, M. Sun, Y. Liu, H. Zhang, Z. Xiong, J. Liang, X. Duan, B. Lai, Nitrogen-doped carbon nanotubes enhanced Fenton chemistry: Role of near-free iron(III) for sustainable iron(III)/iron(II) cycles, Water Res 210 (2022) 117984, https://doi.org/10.1016/j.watres.2021.117984.

[20] J. Wu, J. Wang, C. Liu, C. Nie, T. Wang, X. Xie, J. Cao, J. Zhou, H. Huang, D. Li, S. Wang, Z. Ao, Removal of Gaseous Volatile Organic Compounds by a Multiwalled Carbon Nanotubes/Peroxymonosulfate Wet Scrubber, Environ. Sci. Technol. 56 (2022) 13996–14007, https://doi.org/10.1021/acs.est.2c03590.

[21] Y. Yin, R. Lv, W. Zhang, J. Lu, Y. Ren, X. Li, L. Lv, M. Hua, B. Pan, Exploring mechanisms of different active species formation in heterogeneous Fenton systems by regulating iron chemical environment, Appl. Catal. B: Environ. 295 (2021) 120282, https://doi.org/10.1016/j.apcatb.2021.120282.

[22] Q. Zhang, Y. Peng, Y. Peng, J. Zhang, X. Yuan, J. Zhang, C. Cheng, W. Ren, X. Duan, X. Xiao, X. Luo, Mineralization versus polymerization pathways in heterogeneous Fenton-like reactions, Water Res 249 (2024) 120931, https://doi.org/10.1016/j.watres.2023.120931.

[23] T. Li, C. Chen, A.H. Brozena, J.Y. Zhu, L. Xu, C. Driemeier, J. Dai, O.J. Rojas, A. Isogai, L. Wågberg, L. Hu, Developing fibrillated cellulose as a sustainable technological material, Nature 590 (2021) 47–56, https://doi.org/10.1038/s41586-020-03167-7.

[24] A. Etale, A.J. Onyianta, S.R. Turner, S.J. Eichhorn, Cellulose: A Review of Water Interactions, Applications in Composites, and Water Treatment, Chem. Rev. 123 (2023) 2016–2048, https://doi.org/10.1021/acs.chemrev.2c00477.

[25] C. Yang, Q. Wu, W. Xie, X. Zhang, A. Brozena, J. Zheng, M.N. Garaga, B.H. Ko, Y. Mao, S. He, Y. Gao, P. Wang, M. Tyagi, F. Jiao, R. Briber, P. Albertus, C. Wang, S. Greenbaum, Y. Hu, A. Isogai, M. Winter, K. Xu, Y. Qi, L. Hu, Copper-coordinated cellulose ion conductors for solid-state batteries, Nature 598 (2021) 590–596, https://doi.org/10.1038/s41586-021-03885-6.

[26] K. Xiao, K. Pei, H. Wang, W. Yu, S. Liang, J. Hu, H. Hou, B. Liu, J. Yang, Citric acid assisted Fenton-like process for enhanced dewaterability of waste activated sludge with in-situ generation of hydrogen peroxide, Water Res 140 (2018) 232–242, https://doi.org/10.1016/j.watres.2018.04.051.

[27] Y. Zhang, M. Zhou, A critical review of the application of chelating agents to enable Fenton and Fenton-like reactions at high pH values, J. Hazard. Mater. 362 (2019) 436–450, https://doi.org/10.1016/j.jhazmat.2018.09.035.

[28] F. Wang, W. Dong, Z. Zhao, H. Wang, W. Li, L. Zhang, H. Ouyang, X. Huang, J. Li, Mechanistic insights into Fe(II)-citric acid complex catalyzed CaO_2 Fenton-like process for enhanced benzo[a]pyrene removal from black-odor sediment at circumneutral pH, Water Res 226 (2022) 119233, https://doi.org/10.1016/j.watres.2022.119233.

[29] J. Zhang, H. Song, Y. Liu, L. Wang, D. Li, C. Liu, M. Gong, Z. Zhang, T. Yang, J. Ma, Remarkable enhancement of a photochemical Fenton-like system (UV-A/Fe(II)/PMS) at near-neutral pH and low Fe(II)/peroxymonosulfate ratio by three alpha hydroxy acids: Mechanisms and influencing factors, Sep. Purif. Technol. 224 (2019) 142–151, https://doi.org/10.1016/j.seppur.2019.04.086.

[30] M. Suh, S. Weon, R. Li, P. Wang, J. Kim, Enhanced Pollutant Adsorption and Regeneration of Layered Double Hydroxide-Based Photoregenerable Adsorbent, Environ. Sci. Technol. 54 (2020) 9106–9115, https://doi.org/10.1021/acs.est.0c01812.

[31] Y. Ren, P. Lu, G. Qu, P. Ning, N. Ren, J. Wang, F. Wu, X. Chen, Z. Wang, T. Zhang, M. Cheng, X. Chu, Study on the mechanism of rapid degradation of Rhodamine B with Fe/Cu@antimony tailing nano catalytic particle electrode in a three dimensional electrochemical reactor, Water Res 244 (2023) 120487, https://doi.org/10.1016/j.watres.2023.120487.

[32] J. Dou, Y. Tang, Z. Lu, G. He, J. Xu, Y. He, Neglected but Efficient Electron Utilization Driven by Biochar-Coactivated Phenols and Peroxydisulfate: Polyphenol Accumulation Rather than Mineralization, Environ. Sci. Technol. 57 (2023) 5703–5713, https://doi.org/10.1021/acs.est.3c00022.

[33] H. Zhou, J. Peng, X. Duan, H. Yin, B. Huang, C. Zhou, S. Zhong, H. Zhang, P. Zhou, Z. Xiong, Z. Ao, S. Wang, G. Yao, B. Lai, Redox-Active Polymers as Robust Electron-Shuttle Co-Catalysts for Fast Fe^{3+}/Fe^{2+} Circulation and Green Fenton Oxidation, Environ. Sci. Technol. 57 (2023) 3334–3344, https://doi.org/10.1021/acs.est.2c07447.

[34] F. Lughmani, F. Nazir, S.A. Khan, M. Iqbal, Novel functionalized cellulose derivatives fabricated with Cu nanoparticles: synthesis, characterization and degradation of organic pollutants, Cellulose 29 (2022) 1911–1928, https://doi.org/10.1007/s10570-021-04388-3.

[35] X. Li, C. Li, G. Gao, B. Lv, L. Xu, Y. Lu, G. Zhang, In-situ self-assembly of robust Fe(III)-carboxyl functionalized polyacrylonitrile polymeric bead catalyst for efficient photo-Fenton oxidation of p-nitrophenol, Sci. Total Environ. 702 (2020) 134910, https://doi.org/10.1016/j.scitotenv.2019.134910.

[36] M. Cheng, Z. Qin, J. Hu, Q. Liu, T. Wei, W. Li, Y. Ling, B. Liu, Facile and rapid one–step extraction of carboxylated cellulose nanocrystals by H_2SO_4/HNO_3 mixed acid hydrolysis, Carbohyd. Polym. 231 (2020) 115701, https://doi.org/10.1016/j.carbpol.2019.115701.

[37] H. Hosseini, A. Zirakjou, D.J. McClements, V. Goodarzi, W. Chen, Removal of methylene blue from wastewater using ternary nanocomposite aerogel systems: Carboxymethyl cellulose grafted by polyacrylic acid and decorated with graphene oxide, J. Hazard. Mater. 421 (2022) 126752, https://doi.org/10.1016/j.jhazmat.2021.126752.

[38] S. Ambika, I.M. Nambi, J. Senthilnathan, Low temperature synthesis of highly stable and reusable CMC-Fe^{2+}(-nZVI) catalyst for the elimination of organic pollutants, Chem. Eng. J. 289 (2016) 544–553, https://doi.org/10.1016/j.cej.2015.12.063.

[39] H. Yang, R. Qiu, Y. Tang, S. Ye, S. Wu, F. Qin, L. Xiang, X. Tan, G. Zeng, M. Yan, Carbonyl and defect of metal-free char trigger electron transfer and O_2^- in persulfate activation for Aniline aerofloat degradation, Water Res 231 (2023) 119659, https://doi.org/10.1016/j.watres.2023.119659.

[40] F. Chen, L.L. Liu, J.H. Wu, X.H. Rui, J.J. Chen, Y. Yu, Single-Atom Iron Anchored Tubular g-C_3N_4 Catalysts for Ultrafast Fenton-Like Reaction: Roles of High-Valency Iron-Oxo Species and Organic Radicals, Adv. Mater. 34 (2022) 2202891, https://doi.org/10.1002/adma.202202891.

[41] M. Zhang, C. Xiao, X. Yan, S. Chen, C. Wang, R. Luo, J. Qi, X. Sun, L. Wang, J. Li, Efficient Removal of Organic Pollutants by Metal–organic Framework Derived Co/C Yolk–Shell Nanoreactors: Size-Exclusion and Confinement Effect, Environ. Sci. Technol. 54 (2020) 10289–10300, https://doi.org/10.1021/acs.est.0c00914.

[42] M. Chen, Z. Yan, J. Luan, X. Sun, W. Liu, X. Ke, π-π electron-donor-acceptor (EDA) interaction enhancing adsorption of tetracycline on 3D PPY/CMC aerogels, Chem. Eng. J. 454 (2023) 140300, https://doi.org/10.1016/j.cej.2022.140300.

[43] J. Zhang, B. Xin, C. Shan, W. Zhang, D.D. Dionysiou, B. Pan, Roles of oxygen-containing functional groups of O-doped g-C_3N_4 in catalytic ozonation: Quantitative relationship and first-principles investigation, Appl. Catal. B: Environ. 292 (2021) 120155, https://doi.org/10.1016/j.apcatb.2021.120155.

[44] P. Xu, R. Wei, P. Wang, X. Li, C. Yang, T. Shen, T. Zheng, G. Zhang, $CuFe_2O_4$/diatomite actuates peroxymonosulfate activation process: Mechanism for active species transformation and pesticide degradation, Water Res 235 (2023) 119843, https://doi.org/10.1016/j.watres.2023.119843.

[45] W. Ren, G. Nie, P. Zhou, H. Zhang, X. Duan, S. Wang, The Intrinsic Nature of Persulfate Activation and N-Doping in Carbocatalysis, Environ. Sci. Technol. 54 (2020) 6438–6447, https://doi.org/10.1021/acs.est.0c01161.

[46] L. Lai, P. Zhou, H. Zhou, M. Sun, Y. Yuan, Y. Liu, G. Yao, B. Lai, Heterogeneous Fe (III)/Fe(II) circulation in $FeVO_4$ by coupling with dithionite towards long-lasting peroxymonosulfate activation: Pivotal role of vanadium as electron shuttles, Appl. Catal. B: Environ. 297 (2021) 120470, https://doi.org/10.1016/j.apcatb.2021.120470.

[47] R. Yin, Y. Chen, J. Hu, G. Lu, L. Zeng, W. Choi, M. Zhu, Complexes of Fe(III)-organic pollutants that directly activate Fenton-like processes under visible light, Appl. Catal. B: Environ. 283 (2021) 119663, https://doi.org/10.1016/j.apcatb.2020.119663.

[48] Z. Xie, C. He, H. Zhou, L. Li, Y. Liu, Y. Du, W. Liu, Y. Mu, B. Lai, Effects of Molecular Structure on Organic Contaminants' Degradation Efficiency and Dominant ROS in the Advanced Oxidation Process with Multiple ROS, Environ. Sci. Technol. 56 (2022) 8784–8795, https://doi.org/10.1021/acs.est.2c00464.

[49] Y. Qi, J. Li, Y. Zhang, Q. Cao, Y. Si, Z. Wu, M. Akram, X. Xu, Novel lignin-based single atom catalysts as peroxymonosulfate activator for pollutants degradation: Role of single cobalt and electron transfer pathway, Appl. Catal. B: Environ. 286 (2021) 119910, https://doi.org/10.1016/j.apcatb.2021.119910.

[50] Y. Li, H. Dong, L. Li, J. Xiao, S. Xiao, Z. Jin, Efficient degradation of sulfamethazine via activation of percarbonate by chalcopyrite, Water Res 202 (2021) 117451, https://doi.org/10.1016/j.watres.2021.117451.

[51] M. Che, J. Xiao, C. Shan, S. Chen, R. Huang, Y. Zhou, M. Cui, W. Qi, R. Su, Efficient removal of chloroform from groundwater using activated percarbonate by cellulose nanofiber-supported Fe/Cu nanocomposites, Water Res 243 (2023) 120420, https://doi.org/10.1016/j.watres.2023.120420.

[52] L. Gao, Y. Guo, J. Zhan, G. Yu, Y. Wang, Assessment of the validity of the quenching method for evaluating the role of reactive species in pollutant abatement during the persulfate-based process, Water Res 221 (2022) 118730, https://doi.org/10.1016/j.watres.2022.118730.

[53] Y. Jing, B.P. Chaplin, Mechanistic Study of the Validity of Using Hydroxyl Radical Probes To Characterize Electrochemical Advanced Oxidation Processes, Environ. Sci. Technol. 51 (2017) 2355–2365, https://doi.org/10.1021/acs.est.6b05513.

[54] D. Wang, L. Zhao, H. Ma, H. Zhang, L. Guo, Quantitative Analysis of Reactive Oxygen Species Photogenerated on Metal Oxide Nanoparticles and Their Bacteria Toxicity: The Role of Superoxide Radicals, Environ. Sci. Technol. 51 (2017) 10137–10145, https://doi.org/10.1021/acs.est.7b00473.

[55] L.S. Zhang, X.H. Jiang, Z.A. Zhong, L. Tian, Q. Sun, Y.T. Cui, X. Lu, J.P. Zou, S.L. Luo, Carbon Nitride Supported High-Loading Fe Single-Atom Catalyst for Activation of Peroxymonosulfate to Generate $^1O_2$ with 100% Selectivity, Angew. Chem. Int. Ed. 60 (2021) 21751–21755, https://doi.org/10.1002/anie.202109488.

[56] Z. Wang, E. Almatrafi, H. Wang, H. Qin, W. Wang, L. Du, S. Chen, G. Zeng, P. Xu, Cobalt Single Atoms Anchored on Oxygen-Doped Tubular Carbon Nitride for Efficient Peroxymonosulfate Activation: Simultaneous Coordination Structure and Morphology Modulation, Angew. Chem. Int. Ed. 134 (2022) e202202338, https://doi.org/10.1002/anie.202202338.

[57] Y. Zhang, G. Huang, L.R. Winter, J. Chen, L. Tian, S. Mei, Z. Zhang, F. Chen, Z. Guo, R. Ji, Y. You, W. Li, X. Liu, H. Yu, M. Elimelech, Simultaneous nanocatalytic surface activation of pollutants and oxidants for highly efficient water decontamination, Nat. Commun. 13 (2022) 3005, https://doi.org/10.1038/s41467-022-30560-9.

[58] Y. Lei, Y. Yu, X. Lei, X. Liang, S. Cheng, G. Ouyang, X. Yang, Assessing the Use of Probes and Quenchers for Understanding the Reactive Species in Advanced Oxidation Processes, Environ. Sci. Technol. 57 (2023) 5433–5444, https://doi.org/10.1021/acs.est.2c09338.

[59] J. Wang, Y. Wan, J. Ding, Z. Wang, J. Ma, P. Xie, M.R. Wiesner, Thermal Activation of Peracetic Acid in Aquatic Solution: The Mechanism and Application to Degrade Sulfamethoxazole, Environ. Sci. Technol. 54 (2020) 14635–14645, https://doi.org/10.1021/acs.est.0c02061.

[60] K. Ming, F. Chen, L. Zhu, S. Xia, L. Yang, Z. Shi, L. Deng, H. Zhang, Perborate accelerated copper-immobilized carbon nanofibers activating peroxymonosulfate process for sulfadiazine degradation: Performance and mechanisms understanding, Sep. Purif. Technol. 324 (2023) 124587, https://doi.org/10.1016/j.seppur.2023.124587.

[61] X. Li, J. Jia, J. Zhang, Y. Qin, Y. Wu, M. Zhou, J. Sun, Efficient removal of tetracycline by H_2O_2 activated with iron-doped biochar: Performance, mechanism, and degradation pathways, Chin. Chem. Lett. 33 (2022) 2105–2110, https://doi.org/10.1016/j.cclet.2021.08.054.

[62] M. He, W. Li, Z. Xie, S. Yang, C. He, Z. Xiong, Y. Du, Y. Liu, F. Jiang, Y. Mu, B. Lai, Peracetic acid activation by mechanochemically sulfidated zero valent iron for micropollutants degradation: Enhancement mechanism and strategy for extending applicability, Water Res 222 (2022) 118887, https://doi.org/10.1016/j.watres.2022.118887.

[63] X. Li, X. Wen, J. Lang, Y. Wei, J. Miao, X. Zhang, B. Zhou, M. Long, P.J.J. Alvarez, L. Zhang, CoN_1O_2 Single-Atom Catalyst for Efficient Peroxymonosulfate Activation and Selective Cobalt(IV)=O Generation, Angew. Chem. Int. Ed. 62 (2023) e202303267, https://doi.org/10.1002/anie.202303267.

[64] J. Li, L. Zhao, M. Feng, C. Huang, P. Sun, Abiotic transformation and ecotoxicity change of sulfonamide antibiotics in environmental and water treatment processes: A critical review, Water Res 202 (2021) 117463, https://doi.org/10.1016/j.watres.2021.117463.

[65] J. Peng, P. Zhou, H. Zhou, W. Liu, H. Zhang, C. Zhou, L. Lai, Z. Ao, S. Su, B. Lai, Insights into the Electron-Transfer Mechanism of Permanganate Activation by Graphite for Enhanced Oxidation of Sulfamethoxazole, Environ. Sci. Technol. 55 (2021) 9189–9198, https://doi.org/10.1021/acs.est.1c00020.

[66] B. Zhang, Z. Yan, J. Zhao, Z. Chen, Y. Liu, M. Fan, W. Du, Peroxymonocarbonate activation via Co nanoparticles confined in metal–organic frameworks for efficient antibiotic degradation in different actual water matrices, Water Res 243 (2023) 120340, https://doi.org/10.1016/j.watres.2023.120340.